lengths. Its corresponding radiation pattern is shown in Fig. 2(d). Increasing the antenna length to about 18 wavelengths did not reveal any significant enhancement in antenna gain.

Based on the results of the experiments conducted at *Ku* band, four different antenna structures were scaled and constructed at *V* band. In designing these *V*-band antennas, special attention was given to the possible interface problem between the dielectric insular waveguide and the antenna. The cross-sectional dimension in the interface region was made to have a transition as smooth as possible, such as to minimize any possible mismatch between the dielectric waveguide and the antenna. The various configurations are shown in Fig. 3 together with their pattern and gain measurements. The highest gain obtained is 15.2 dB corresponding to the measured radiation pattern of Fig. 3(b).

In general, the empirical results agree well with the design formulas given by (1) and (2). It was found that for a given relative dielectric constant, the optimum radiation characteristics can be obtained if the cross-sectional dimension d_{max} is properly chosen. For HI-K707L material, a dimension of $d_{max}/\lambda_0 \approx 0.2$ was observed to provide the maximum gain. The gain of a dielectric rod is initially increased by increasing the antenna length. However, the relationship is not linear. For sufficiently long length, a considerable increase in antenna length will not result in a corresponding increase in the gain of the antenna. Instead, a slight decrease in antenna gain had been noticed after about 14 wavelengths in some antenna configurations investigated. The maximum gain realized was about 18 dB at *Ku* band and 15.2 at *V* band.

IV. Concluding Remarks

The effort to design a millimeter-wave antenna suitable for millimeter-wave integrated-circuit applications has been described. The results of these measurements were evaluated. The antenna of Fig. 3(b) was selected as the most suitable configuration for this MILIC application. This antenna was fabricated and integrated directly into the transmitter and the receiver modules as an easily replaceable component [9]. The antenna is bonded to a T-shaped fixture which is fastened to the main plate with two screws. The insular waveguide on the antenna fixture and main plate are butted together to form a continuous energy path. Since the dielectric antenna protrudes out of the transmitter case, a protective polystyrene radome has been provided in order to prevent breakage. The addition of a single radome adds approximately 0.2-dB loss to the overall system. The receiver module [9] used the same dielectric rod antenna. The receiver antenna is also replaceable in case of damage and is protected by a polystyrene radome.

To provide a higher gain for MILIC technology, the consideration of possible alternative techniques with regard to millimeter-wave integrated-circuit applications and requirements is being considered. A detailed discussion on the empirical results described previously and the limitations of the existing concepts of utilizing a simple dielectric rod for MILIC applications has been reported elsewhere [4].

Acknowledgment

The author wishes to thank A. R. Valentino and A. Kaurs of the IIT Research Institute for their many helpful discussions during the course of this work.

References

[1] E. A. J. Marcatili, "Dielectric rectangular waveguide and directional coupler for integrated optics," *Bell System Technical Journal*, vol. 48, no. 7, pp. 2079–2102, Sept. 1969.
[2] R. M. Knox and P. P. Toulios, "Integrated circuits for the millimeter through optical frequency range," *Proc. of the Symposium on Submillimeter Waves*, New York, March 31–April 2, 1970.
[3] P. P. Toulios and R. M. Knox, *Image Line Integrated Circuits for System Applications at Millimeter Wavelengths*, U.S. Army Electronics Command, Contract ECOM-73-0217-F, July 1974.
[4] B. J. Levin and J. E. Kietzer, *Hybrid Millimeter-Wave Integrated Circuits*, U.S. Army Electronics Command, Contract ECOM-74-0577-F, Oct. 1975.
[5] D. G. Kiely, *Dielectric Aerials*. London, England: Methuen and Co., Ltd., 1952.
[6] G. E. Mueller and W. H. Tyrrell, "Polyrod antennas," *Bell System Technical Journal*, vol. 26, p. 837.
[7] F. E. Butterfield, "Dielectric sheet radiators," *IRE Trans. Antennas Propag.*, p. 152, Oct. 1954.
[8] G. C. Southworth, "Principles and applications of waveguide transmission," *Bell Laboratories Series D*, Van Nostrand Co., Inc., Princeton, NJ, 1950.
[9] J. E. Kietzer, A. R. Kaurs, and B. J. Levin, "A *V*-band communication transmitter and receiver system using dielectric waveguide integrated circuits," this issue, pp. 797–803.

E-Type Modes in Cylindrical Dielectric Waveguides with Periodic Boundary Perturbations

ERCAN TOPUZ, MEMBER, IEEE

***Abstract*—A general method for the analysis of the effects of periodic boundary perturbations on *E*-type modes of dielectric waveguides (DW's) is presented. The method is applied to hollow cylindrical dielectric waveguide (HCDW), and numerical solutions for surface wave and radiation mode intensities are given.**

The effects of periodic boundary perturbations on *E*-type modes of dielectric waveguides (DW's) have not been investigated. Existing asymptotic approximations [1]–[4] are only valid in the optical region, where core-cladding refractive index differences are orders of magnitude smaller than in the millimeter region. In the present short paper we extend the work of Marcuse and Derosier [5], [6] for *H*-type modes of DW to include *E*-type modes and, taking hollow cylindrical dielectric waveguide (HCDW) as a specific example, give approximate solutions of surface wave and radiation intensities.

HCDW is shown in Fig. 1 with sinusoidally perturbed boundaries. The modes of the unperturbed guide are well known [7]. *E*-type modes exist only in case of cylindrical symmetry, and with $H_\phi = h_\phi \exp \pm j\beta z$ we have for surface wave modes

$$h_{\phi m} = \begin{cases} j\omega\varepsilon_0/\Gamma_m C_{1m} I_1(\Gamma_m r), & r < a_1 \\ j\omega\varepsilon_0\varepsilon_r/\Omega_m [C_{2m} J_1(\Omega_m r) + D_{2m} Y_1(\Omega_m r)], & a_1 < r < a_2 \\ -j\omega\varepsilon_0/\Gamma_m D_{3m} K_1(\Gamma_m r), & r > a_2 \end{cases}$$

and for radiation modes

$$h_\phi = \begin{cases} j\omega\varepsilon_0/\bar{\Omega}_1 A_1 J_1(\bar{\Omega}_1 r), & r < a_1 \\ j\omega\varepsilon_0\varepsilon_r/\bar{\Omega}_2 \{A_2 J_1(\bar{\Omega}_2 r) + B_2 Y_1(\bar{\Omega}_2 r)\}, & a_1 < r < a_2 \\ j\omega\varepsilon_0/\bar{\Omega}_3 \{A_3 J_1(\bar{\Omega}_3 r) + B_3 Y_1(\bar{\Omega}_3 r)\}, & r > a_2 \end{cases} \quad (2)$$

where J_1 and Y_1 are Bessel functions, I_1, K_1 are modified Bessel functions of the first and second kind and of the first order, Γ and Ω are radial propagation constants given as

$$\Gamma_m = \sqrt{\beta_m^2 - k_0^2} \qquad \Omega_m = \sqrt{\varepsilon_r k_0^2 - \beta_m^2}$$
$$\bar{\Omega}_3 = \bar{\Omega}_1 = \sqrt{k_0^2 - \bar{\beta}^2} \qquad \bar{\Omega}_2 = \sqrt{\varepsilon_r k_0^2 - \bar{\beta}^2} \quad (3)$$

A,B,C,D, are integration constants, and exp ($j\omega t$) time dependence is assumed. Normalizing these modes to carry the same

Manuscript received February 4, 1976; revised June 1, 1976.
The author is with the ITU Electrical Engineering Factory, Gumussuyu, Istanbul, Turkey.

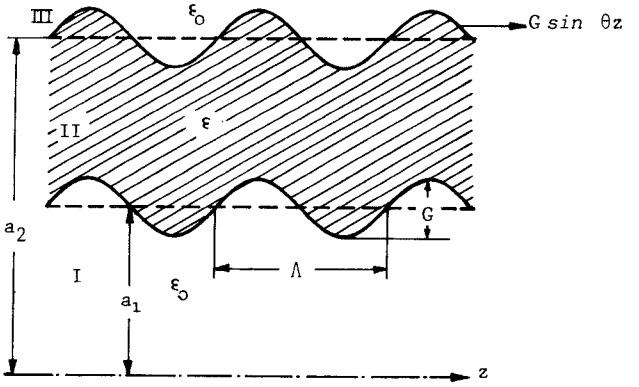

Fig. 1. HCDW with sinusoidally perturbed boundaries.

power P, we obtain a complete set of normalized orthogonal functions for circularly symmetric fields.

We will first assume a simple sinusoidal surface roughness on the boundaries of HCDW defined with parameters shown in Fig. 1. In this case the dielectric constant can be expressed as

$$\varepsilon(r,z) = \varepsilon_0\{\varepsilon_{r0}(r) + \Delta\varepsilon(r,z)\} \tag{4}$$

where $u(\cdot)$ is the unit step function

$$\varepsilon_{r0}(r) = 1 + (\varepsilon_r - 1)u(r - a_1) + (1 - \varepsilon_r)u(r - a_2) \tag{5}$$

the dielectric constant of the unperturbed guide

$$\Delta\varepsilon(r,z) = (\varepsilon_r - 1)[u(r - r_1) - u(r - a_1)] + (1 - \varepsilon_r)[u(r - r_2) - u(r - a_2)] \tag{6}$$

$$r_1 = a_1 + G\sin\theta z$$

$$r_2 = a_2 + G\sin\theta z \tag{7}$$

and small amplitude perturbation is assumed, i.e., $G \ll a_1,\Lambda$. With the aid of (4)–(7) the scalar wave equation for E-type modes of the perturbed guide can be obtained as

$$\nabla^2 H_\phi - \frac{1}{r^2} H_\phi + \omega^2\mu_0(\varepsilon_{r0} + \Delta\varepsilon)\varepsilon_0 H_\phi = \frac{\varepsilon_0(\varepsilon_r - 1)}{\varepsilon r}\{\delta(r - r_1) - \delta(r - r_2)\} \cdot \left\{\sin|\gamma| r\frac{\partial H_\phi}{\partial z} + \cos\gamma\frac{\partial}{\partial r}(rH_\phi)\right\} \tag{8}$$

where $\gamma = \arctan(G\theta\cos\theta z)$.

This equation will now be solved with the method of expansion in normal modes. Since our analysis follows closely that of Marcuse, only the end results will be given. We will enter (8) with the expansion

$$H_\phi = \sum_1^N F_n(z)H_{\phi n} + \int_0^\infty f(\bar{\Omega},z)H_{\phi\Omega}\,d\bar{\Omega} \tag{9}$$

where $F_n(z)$ and $f(\Omega,z)$ are expansion coefficients of surface wave and radiation modes, respectively, the first term on the right-hand side covers the finite [7] discrete spectrum of surface waves, and the second term covers the continuous spectrum of the radiation modes. Using orthogonality and periodicity [5] conditions, formal solutions for the expansion coefficients are obtained in the form of integral equations which can be divided into components associated with waves traveling in + and $-z$ directions, and can be evaluated numerically by successive iterations once a suitable perturbation model is chosen. We will assume that the perturbed guide is terminated in its characteristic impedance on both sides, and that only the dominant surface wave mode traveling in + z direction is incident to the perturbation region. We further assume that the perturbation length l is such that

$$l \gg \lambda_0,\Lambda$$

$$\Delta P_r \ll P \tag{10}$$

where λ_0 is the free-space wavelength, Λ is the perturbation wavelength, and ΔP_r is the total power coupled to radiation modes. Under these assumptions, the first-order solution to an expansion coefficient corresponding to mth surface wave mode traveling in $+z$ direction and satisfying resonance condition, i.e., $\beta_1 - \beta_m = \theta = 2\pi/\Lambda$, becomes after it has traveled a distance l in the HCDW

$$F_m(l)^+ = \frac{\pi}{2\omega\varepsilon_0\varepsilon_{r0}P}\frac{\varepsilon_r - 1}{\varepsilon_r}\frac{Gl}{2}\left\{k_0^2\varepsilon_r r h_{\phi 1}h_{\phi m}^*\Big|_{a_2}^{a_1} + \frac{d}{dr}\frac{d}{dr}\cdot(rh_{\phi 1})h_{\phi m}^*\Big|_{a_1}^{a_2} S_1 - j\beta_1\frac{d}{dr}(rh_{\phi 1}h_{\phi m})\Big|_{a_1}^{a_2} T_1\right\} \tag{11}$$

where

$$S_1 = \frac{2}{\pi p}\left\{\frac{1 + p^2}{p}\arctan p - 1\right\}$$

$$T_1 = \frac{4\sqrt{1 + p^2}}{\pi p^2}\{F(p/\sqrt{1 + p^2}) - E(p/\sqrt{1 + p^2})\}. \tag{12}$$

$p = G\theta$, $E(\cdot)$ and $F(\cdot)$ are complete elliptic integrals of the first and second kind. Due to the adopted normalization, the power coupled to this mode will simply be $P|F_m(l)^+|^2$. At a distance l_0 where $|F_m(l_0)^+|^2 = 1$ total power exchange will take place. In Fig. 2 normalized perturbation lengths for 100-percent power coupling between first and second surface wave modes are given for various values of a_2/a_1.

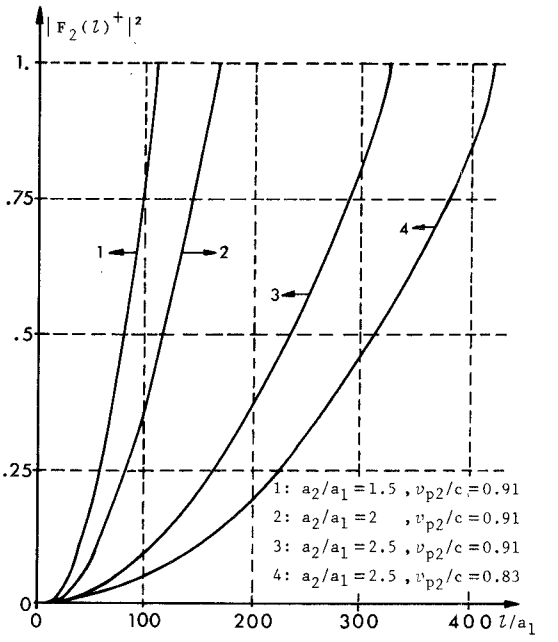

Fig. 2. The change of the relative power coupled to the second surface wave mode versus relative perturbation length. $G/a_1 = 10^{-2}$, $\varepsilon_r = 1.99$.

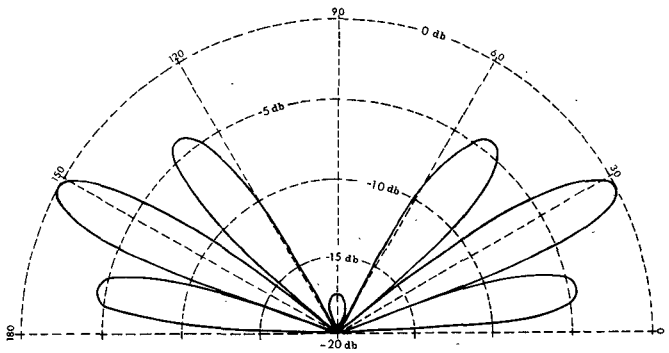

Fig. 3. Far-field radiation pattern of the HCDW. 0 dB = $5\ 10^{-3}\ l/a_1 W$, $a_2/a_1 = 1.5$, $G/a_1 = 5\ 10^{-3}$, $v_{p1}/c = 0.77$, $\varepsilon_r = 1.99$.

The fractional power coupled to the radiation modes traveling in the $+z$ direction can be expressed as

$$\begin{aligned}\frac{\Delta P_{r1}^{+}}{P} = X_3 \Bigg\{ & S_1^2 \frac{c^2}{v_{p1}^2}\left(\frac{c^2}{v_{p1}^2}-1\right)\Bigg\{ I_0(\Gamma a_1)J_1(\bar{\Omega}_1 a_1) \\ & + \frac{\bar{\Omega}_1}{\Gamma} I_1(\Gamma a_1)\left[J_0(\bar{\Omega}_1 a_1) - \frac{J_1(\bar{\Omega}_1 a_1)}{\bar{\Omega}_1 a_1}\right] \\ & + \frac{\bar{\Omega}_1}{\Gamma}\frac{a_2}{a_1}\frac{D_3}{C_1} K_1(\Gamma a_2)\left[X_1 - \frac{X_2}{\bar{\Omega}_1 a_2}\right] \\ & - \frac{a_2}{a_1}\frac{D_3}{C_1} K_0(\Gamma a_2) X_2\Bigg\}^2 \\ & + \Bigg\{ T_1 \Bigg\{ \frac{\Gamma^2}{k_0^2} I_1(\Gamma a_1)J_1(\bar{\Omega}_1 a_1) \\ & - \frac{a_2}{a_1}\frac{D_3}{C_1} K_0(\Gamma a_2)\frac{\Gamma\bar{\Omega}_1}{k_0^2} X_1 + \frac{\Gamma^2}{k_0^2}\frac{a_2}{a_1}\frac{D_3}{C_1} K_1(\Gamma a_2) X_2\Bigg\} \\ & + \varepsilon_r I_1(\Gamma a_1)J_1(\bar{\Omega}_1 a_1) \\ & + \varepsilon_r \frac{a_2}{a_1}\frac{D_3}{C_1} K_1(\Gamma a_2) X_2\Bigg\}^2\Bigg\} \end{aligned} \tag{13}$$

where

$$X_1 = \frac{A_3}{A_1} J_0(\bar{\Omega}_1 a_2) + \frac{B_3}{A_1} Y_0(\bar{\Omega}_1 a_2)$$

$$X_2 = \frac{A_3}{A_1} J_1(\bar{\Omega}_1 a_2) + \frac{B_3}{A_1} Y_1(\bar{\Omega}_1 a_2)$$

$$X_3 = 4\pi^7 \frac{l}{p^2}\frac{G}{\lambda_0}\left(\frac{a_1}{\lambda_0}\right)^3 \varepsilon_0^2 \left(\frac{\varepsilon_r - 1}{\varepsilon_r}\right)^2 \frac{\omega^2 \bar{\beta} C_1^2}{\Gamma^2 \bar{\Omega}_1^3 A_1^2}$$

$$\bar{\beta} = \beta_1 - \theta. \tag{14}$$

The powers coupled to waves propagating in the reverse direction can simply be obtained from (11) and (13) by replacing β with $-\beta$ and modifying (12) and (14) correspondingly. At this point it is convenient to introduce a real angle ψ, defined as $\Psi = \arccos \bar{\beta}/k_0$, which can be interpreted as the angle between the guide axis and the direction of the maximum radiation of the far field. An example of the numerically computed far-field radiation pattern is given in Fig. 3. It must be noted that changing

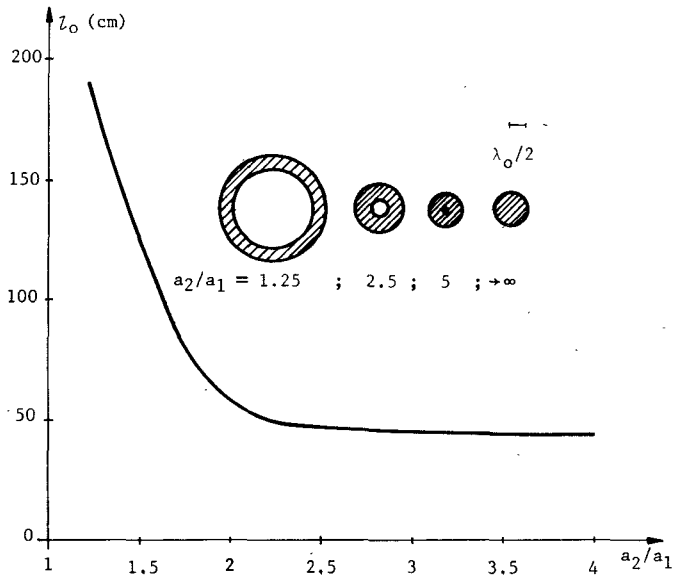

Fig. 4. The change of perturbation length for 100-percent power coupling between the first and second surface wave modes of HCDW. $v_{p1}/c = 0.79$, $\varepsilon_r = 1.99$, $\Lambda = 1.93$ cm, $G = 1.65\ 10^{-3}$ cm, $f = 60$ GHz.

ψ in Fig. 3 has to be understood as a corresponding change either in the geometry of the guide or in frequency so that

$$\frac{\lambda_0}{\Lambda} = \frac{c}{v_{p1}} \pm \cos\psi, \qquad \begin{matrix} - \text{ for } 0 \le \psi \le \pi/2 \\ + \text{ for } \pi/2 \le \psi \le \pi. \end{matrix}$$

It is obvious that any circularly symmetric periodic disturbance on the boundaries of the guide can be treated in the same manner by simply applying (11) and (13) to each significant Fourier component of the disturbing function. On the other hand, the effects of periodic boundary perturbations on E-type modes of the dielectric rod and of the dielectric slab waveguides can also be obtained from the preceding analysis. The necessary modification is straightforward. For the case of the dielectric rod it is sufficient to replace (7) by

$$\begin{aligned} r_1 &= a_1 \\ r_2 &= a_2 + G \sin\theta z \end{aligned} \tag{15}$$

and go to the limit $a_2/a_1 \to \infty$ as the phase velocity of the incident mode (v_{p1}) is kept constant at the value of interest. The limit $a_2/a_1 \to 1$, v_{p1} = constant will result in dielectric slab waveguide perturbed on one or both sides depending on whether (7) or (15) is chosen as the disturbing function. The numerical results of such an analysis are presented in Fig. 4 together with the change of the geometry. It is evident from Fig. 4 that in terms of power lost to higher order modes, HCDW occupies a place between the dielectric slab and dielectric rod waveguides, its relative position depending on its geometry. Our results compare very well with the existing data [2] and suggest that E-type modes of DW are slightly more lossy [6].

References

[1] A. W. Snyder and E. DeLaRue, "Asymptotic solutions of eigenvalue equations for surface waveguide structures," *IEEE Trans. Microwave Theory Tech.*, pp. 650–651, Sept. 1970.
[2] D. Marcuse, "Radiation losses of tapered slab waveguides," *B.S.T.J.*, pp. 273–290, Feb. 1970.
[3] C. Elachi and C. Yeh, "Periodic structures in integrated optics," *J. App. Phys.*, pp. 3146–3151, July 1973.
[4] S. T. Peng, T. Tamir, and H. L. Bertoni, "Theory of periodic dielectric waveguides," *IEEE Trans. Microwave Theory Tech.*, pp. 123–133, Jan. 1975.
[5] D. Marcuse, "Mode conversion caused by surface imperfections of a dielectric slab waveguide," *B.S.T.J.*, pp. 3187–3215, Dec. 1969.

[6] D. Marcuse and R. M. Derosier, "Mode conversion caused by diameter changes of a round dielectric waveguide," *B.S.T.J.*, pp. 3216–3233, Dec. 1969.
[7] E. Topuz, "Periodic boundary perturbations on cylindrical dielectric waveguides," Diss. I.T.U., Istanbul, 1975.

A Tunable Bandpass Ring Filter for Rectangular Dielectric Waveguide Integrated Circuits

ALLAN R. KAURS, MEMBER, IEEE

Abstract—**Dielectric waveguide structures have received renewed interest in recent years for application at millimeter wavelengths. A number of passive and active microwave devices in the dielectric waveguide technologies have been recently developed. This short paper describes a method for providing continuous mechanical tuning of a resonant dielectric ring filter for use with rectangular dielectric waveguide integrated circuits. Results obtained with an experimental device operating at *K* band are also given.**

I. Introduction

A bandpass filter can be constructed using a dielectric ring of rectangular cross section that is proximity-coupled to two dielectric image waveguides which form the input and output lines of this four-port device. The ring is a multiple resonant bandpass device which will provide a maximum transfer of microwave energy from one line to the other at center frequencies where the mean circumference of the ring is approximately $n\lambda g$ ($n = 1,2,3,\cdots$). The basic analytical approach and some practical applications of these types of filters can be found in [1]–[4].

The resonant condition for the ring of $n\lambda g$ was stated to be only approximate because the propagation characteristics of the uncoupled portion of the loop are different, in general, from that of the coupled sections. The propagation characteristics are therefore a function of various physical parameters such as overall dimensions and loading. The basic ring configuration provides fixed-frequency responses with the center frequencies primarily determined by the ring filter dimensions. Consequently, a great deal of tolerance must be achieved in machining the rings in order to obtain filters with the desired resonant frequencies. This limitation led to the development of the tunable filter described in this short paper. The tuning characteristic is achieved by controlling or changing the effective guide wavelenth around the ring.

It is known that the dispersion characteristics of insulated image guide are a function of the thickness of the low-permittivity dielectric layer used to suspend the high dielectric constant waveguide off the metal ground plane. Theoretical curves demonstrating this dependence for straight sections of insulated image guide can be found in [4]. These curves demonstrate that there can be significant variation in the guide dispersion characteristics as the low-permittivity layer thickness approaches zero. It is this dependence of guide wavelength on the thickness of the substrate layer for a fixed waveguide structure that is proposed to be used in tuning the ring filter.

II. An Experimental Tunable Bandpass Filter

An experimental tunable bandpass filter was constructed for *K*-band operations. The tunable filter consists of a dielectric ring mounted in a bandpass configuration between two sections of dielectric waveguide which form the input and output feed lines. The ring structure rides on a piston which is spring-loaded and mounted in the metal base plate. A tuning screw is mounted above the ring, which is used to control the piston movement and, in turn, the gap between the ring and baseplate. A cross-sectional sketch of the device is shown in Fig. 1. The experimental device utilizes a variable air gap ($\varepsilon_r = 1.0$) beneath the ring instead of a dielectric material layer.

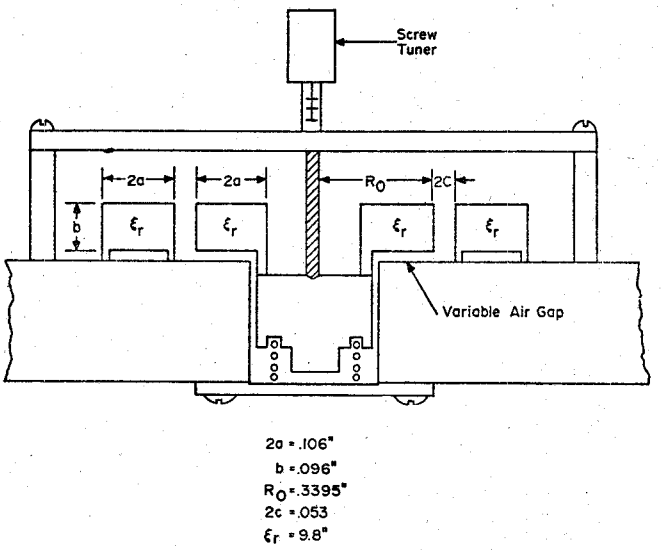

Fig. 1. A cross section of a tunable MILIC bandpass filter.

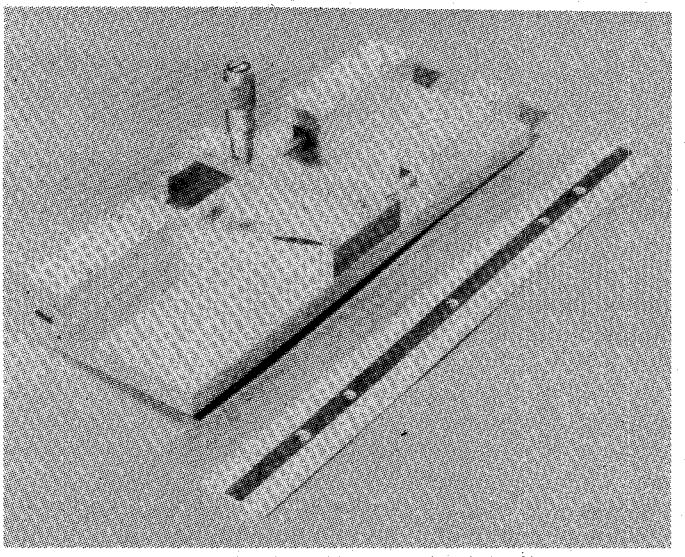

Fig. 2. A *K*-band tunable MILIC bandpass filter.

Fig. 2 is a photograph of the experimental *K*-band filter mounted on a test plate. The dielectric ring can be seen in the center of the test plate with the micrometer tuning screw mounted above. Three of the output ports of the device are fed into standard metal-waveguide-to-dielectric-image-guide launchers for the connection of test equipment. The fourth port is terminated with a ferrite load.

The material used for the dielectric guides and ring structure was Custom Materials High-K 707L with a dielectric constant of $\varepsilon_r = 9.8$. This plastic material has a higher loss tangent than alumina ceramic, but it is much easier to machine and work with for laboratory prototypes.

Manuscript received February 24, 1976; revised May 20, 1976. This work was supported by the U.S. Air Force Flight Dynamics Laboratory, Dayton, OH, under Contract F33615-75-R-3100.
The author is with IIT Research Institute, Chicago, IL 60616.